Atomistic simulation for deforming complex alloys with application toward TWIP steel and associated physical insights

Peng Wang[a], Shaofeng Xu[a], Jiabin Liu[b], Xiaoyan Li[c], Yujie Wei[d], Hongtao Wang[a,*], Huajian Gao[e,*], Wei Yang[a,*]

[a] Institute of Applied Mechanics, Zhejiang University, Hangzhou 310027, China
[b] College of Materials Science and Engineering, Zhejiang University, Hangzhou 310027, China
[c] Department of Engineering Mechanics, Tsinghua University, Beijing 100084, China
[d] LNM, Institute of Mechanics, Chinese Academy of Sciences, Beijing 100190, China
[e] Division of Engineering, Brown University, Providence, RI 02912, USA

ARTICLE INFO

ABSTRACT

The interest in promoting deformation twinning for plasticity is mounting for advanced materials. In contrast to disordered grain boundaries, highly organized twin boundaries are beneficial to promoting strength-ductility combination. Twinning deformation typically involves the kinetics of stacking faults, its interplay with dislocations, as well as the interactions between dislocations and twin boundaries. While the latter has been intensively studied, the dynamics of stacking faults has been rarely touched upon. In this work, we report new physical insights on the stacking fault dynamics in twin induced plasticity (TWIP) steels. The atomistic simulation is made possible by a newly introduced approach: meta-atom molecular dynamics simulation. The simulation suggests that the stacking fault interactions are dominated by dislocation reactions that take place spontaneously, different from the existing mechanisms. Whether to generate a single stacking fault, or a twinning partial and a trailing partial dislocation, depends upon a unique parameter, namely the stacking fault energy. The latter in turn determines the deformation twinning characteristics. The complex twin-slip and twin-dislocation interactions demonstrate the dual role of deformation twins as both the dislocation barrier and dislocation storage. This duality contributes to the high strength and high ductility of TWIP steels.

1. Introduction

Understanding the deformation mechanisms of crystals is not only scientifically interesting but also of technological importance in developing materials with novel mechanical properties (Jacobsen and Schiotz, 2002; Yip, 2004). Simplified material "models" that capture the essences of deformation play a critical role. Bragg and Nye developed a bubble raft model which unveiled the "atomic" arrangements of dislocations and grain boundaries (GB) in polycrysts (Bragg and Nye, 1947). In spite of large simplifications, the bubble raft model successfully captured the dynamic behaviors of dislocation nucleation and GB migration during plastic deformation (Georges et al., 1986; Gouldstone et al., 2001). The ever-increasing computation power enables us to realize the massively parallel molecular-dynamics (MD) simulations to capture realistic and material-specific deformations. The embedded atom method (EAM) (Daw and Baskes, 1983, 1984) and Finnis-Sinclair potentials (EAM-FS) (Finnis and Sinclair, 1984) took into account the local electron density and pairwise interactions in a semi-empirical way. Many successes were reported for its modeling

---

on the deformation behaviors of nano-crystals (Li et al., 2010, 2009; Van Swygenhoven et al., 2004a; Van Swygenhoven and Weertman, 2006; Yamakov et al., 2004; Zhou et al., 1998). For example, MD simulations have led to a deformation mechanism map for representative single-element, face-centered-cubic (FCC) nano-crystals in terms of the average grain size and external stress (Yamakov et al., 2004). With rapidly growing interests in multi-element and multi-component metallic alloys, including the high entropy alloys (Gludovatz et al., 2014; Zhang et al., 2014), the development of interatomic potentials has lagged behind the computational power. This problem arises partly due to the intrinsic difficulty of the existing methods in constructing pairwise interaction terms in the interatomic potential, which becomes almost intractable even for ternary alloy systems.

In contrast, the Ashby-type deformation mechanism maps have been widely adopted for guiding material designs and applications since 1970s (Ashby, 1972). The basic principle of such representations is to use mechanism-based constitutive equations to divide the deformation-parameter space into regions where a single mechanism becomes rate controlling (Yamakov et al., 2004). The deformation-parameter space usually consists of two of the three normalized parameters: stress, temperature and grain size. The underlying idea is that macroscopic mechanical responses are dictated by only a few key parameters, such as the lattice constant, the surface energy, the stable and unstable stacking fault energies, the elastic moduli, the sublimation energy, the vacancy formation energy, the microstructure parameters, and the temperature. Most of the specific atomic details can be neglected so that the physical processes during alloy deformation can be depicted by simplified models with essentially the same collective behaviors. With this principle in mind, we propose an EAM-based meta-atom molecular dynamics (MAMD) method to simulate the mechanical deformation of metallic alloys. By this approach and simplified interatomic potentials, massively parallel atomistic simulations of three-dimensional polycrystals are amenable to explore the deformation mechanisms in twinning-induced-plasticity (TWIP) steel, an alloy system with practical importance and broad applications. The prevalence of deformation twinning in TWIP steel leads to both high strength and exceptional formability for industrial applications. We will show that MAMD simulation is capable of capturing the microstructures and the typical deformation characteristics of TWIP steel as observed in experiments. It enables us to probe the parametric dependence of deformation mechanisms, indicating potential applications in designing the alloy with prescribed mechanical properties.

2. Development of meta-atom method

2.1. Basic assumptions

The proposed meta-atom method is based on the following conjecture: the mechanical properties of an alloy system are primarily governed by a finite set of material constants, such as the lattice constants, the surface energy, the stable and unstable stacking fault energies (SFE), the elastic moduli, the sublimation energy and the vacancy formation energy. Once the completeness of this set of material constants is established, two systems with the same material constants should exhibit identical mechanical behaviors in experimental observations. In this way, a detailed distinction among various atomic species is discarded and an alloy system is represented by a set of meta-atoms with a single interatomic potential to fit all related material constants. The essence of this homogenization methodology lies with the assumption that there exists a length scale at which the behaviors of two systems are governed by the same set of measurable materials properties, in spite of the difference and inhomogeneity in an atomic scale.

Based on the above assumptions, the atomic interaction among meta-atoms is formulated based on the EAM-FS potential (Finnis and Sinclair, 1984; Johnson, 1989):

$$U_i = F(\rho_i) + \frac{1}{2}\sum_{j \neq i} \phi(r_{ij})$$

(1)

where $F(\rho_i)$ is the embedding energy of the i-th meta-atom, $\phi(r_{ij})$ the pair potential between meta-atoms i and j, and ρ_i the local electron density furnished by the remaining atoms in the system. More details about the EAM potential can be found in the review by Daw et al. (1993). The universality of the EAM potential provides adequate flexibility in constructing model materials with properties varying in a sufficiently large range, covering spectra of different classes of metallic alloys. We note that the MAMD method follows the conventional MD procedures and cannot account for processes whose transition times exceed microseconds. Recently, a collection of algorithms including the potential energy surface sampling method has been successfully employed to assess the mechanical behavior of a nanopillar under strain rate from 1 to 10^8 s^{-1} (Fan et al., 2013; Yan et al., 2015; Yan and Sharma, 2016). This algorithm can be adopted by the MAMD method, which is under future investigation.

We followed the established method of Ackland et al. (1997), Mendelev et al., (2003, 2008) and Mendelev and Srolovitz (2002) to develop meta-atom potentials. The embedding function and the pair function are formulated by superposition of basis polynomial functions:

$$F(\rho) = a_1\sqrt{\rho} + a_2\rho^2 + a_3\rho^4 + H(\rho - 40)\cdot0.1\cdot(\rho - 40)^2$$

(2)

$$\phi(r) = \left(\sum_{i=0}^{2} b_i r^i\right)\cdot H(r_0 - r) + H(r - r_0)\sum_{i=1}^{N}\sum_{p=3}^{4} c_{i,p}(r_i - r)^p H(r_i - r)$$

(3)

where $H(r)$ is the Heaviside function, N the number of basic functions and a_i, b_i, $c_{i,p}$ and r_i the fitting coefficients. We used 8 knots for the pair function. The ρ function is adopted from Mendelev et al. (2003), which accurately reproduces the crystallinity, the melting properties, and the liquid structure of iron. The cutoff distance is chosen as r_{cut}=1.65 a_0. The pair function and density
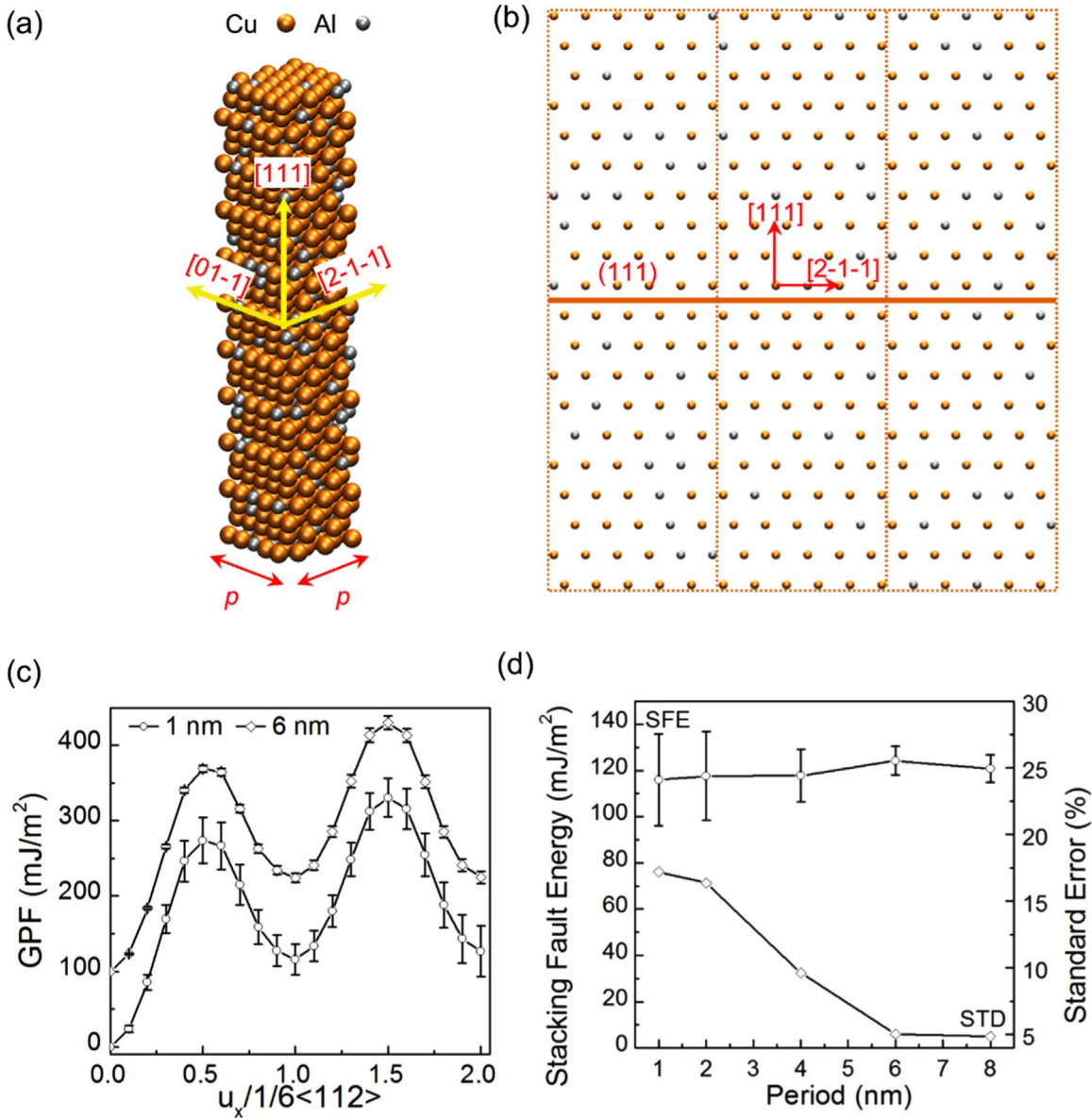
Fig. 1. (a) Atomic model for MD simulation of aluminum bronzes (Cu-6 wt% Al). The simulation box period is denoted as *p*. (b) The simulation system is projected along [01-1]. The dashed line and the solid line indicate the simulation box and the slip plane, respectively. (c) The generalized planar fault (GPF) energy curves for simulation boxes with periods of 1 nm and 6 nm. The curves are shifted from each other for clarity. (d) The variation of SFE with the simulation box period.

function are forced to be 0 at a cutoff distance. The knots and coefficients for the meta-atom potential of selected TWIP steel are provided in Tables A1 and A2 (see Appendix), respectively.

2.2. Applicability

The plastic deformation mechanisms of metals have close relation to the generalized planar fault (GPF) energy curve, which represents the energy cost of rigidly shifting two semi-infinite blocks of the crystal on a (111) plane along $<112>$ direction (Fig. 1(a) and (b)). The applicable size regime of the meta-atom method can be defined by considering the fluctuation in GPF curves due to the chemical inhomogeneities in alloys. To demonstrate this, we take aluminum bronzes as the model system for the available EAM potentials. The interatomic EAM potentials from Liu et al. (1999) are used to model Cu-Cu, Cu-Al and Al-Al interactions. Fig. 1(c) shows the GPF curves for the atomic models of Cu-6 wt% Al with simulation box periods (*p*) of 1 nm and 6 nm, respectively. A variation in GPF energy is observed from test to test due to the local atomic arrangements near the slip plane. One may observe that the average SFE is nearly independent of the box period, while the errors are reduced to 10% when $p > 4$ nm and 5% when $p >$
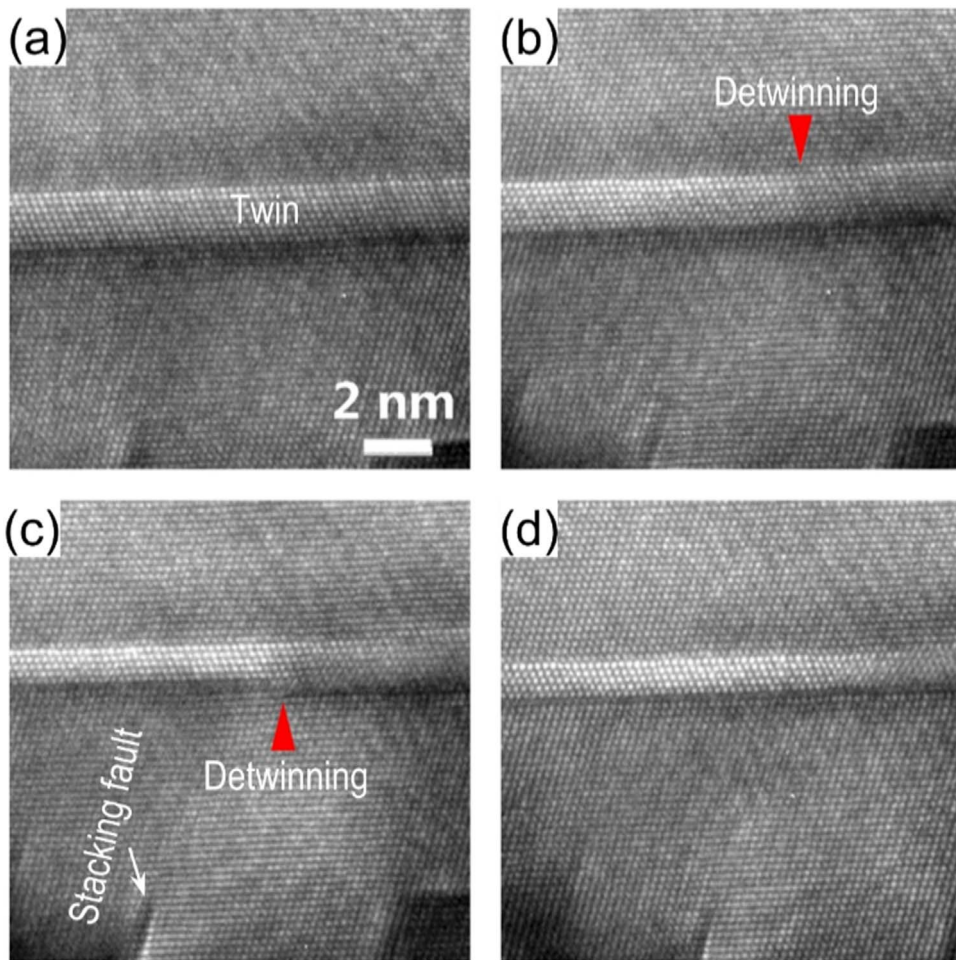
Fig. 2. Sequential snapshots showing the de-twinning process in Cu-6 wt% Al alloys as recorded by the *in-situ* transmission electron microscopy observation. (a) Atomic resolution twin structure in the alloy. (b) and (c) Gliding twin partials along the twin boundaries (TBs). (d) The twin structure with smaller thickness.

6 nm, suggesting a critical length scale of 4–6 nm (Fig. 1(d)). The MD simulation on Cu-1 wt% Al gives the same length scale in calculating average material properties (not shown here).

The above observation shows the convergence of the length scales for calculating material properties with different compositions. On the other hand, alloys resemble the exact atomic arrangements of microstructures as pure metals composed of meta-atoms. One example is given in Fig. 2, which shows sequential snapshots of *in-situ* transmission electron microscopy (TEM) observation on the tensile deformation of a piece of Cu-6 wt% Al alloy with atomic resolution. The lattice fringe reflects the average electron scattering from atom columns containing both Cu and Al atoms. The twinning and de-twinning processes, as well as the motion of stacking faults, are frequently observed, as recognized in metals with low stacking fault energies (Rohatgi et al., 2001; Zhang et al., 2009). Clearly, the microstructures, such as the twin in (a) and stacking faults in (c), share the same crystallography characteristics as those in pure metals. This experimental evidence indicates that the atomic details of deformation mechanisms can be represented by meta atoms.

3. MAMD simulations of TWIP steels

3.1. Meta-atom potential for TWIP steel

Fig. 3(a–c) plot the meta atom potential for a TWIP steel with composition of Fe-22 wt%Mn-0.6 wt%C (Cooman et al., 2011; Ghasri-Khouzani and McDermid, 2015; Pierce et al., 2014). Table 1 lists the material properties. To model crystal plasticity, the embedding function and the pair potential are optimized to fit the following parameters: lattice constants, elastic moduli (C_{11}, C_{12} and C_{44} for crystal with cubic symmetry), SFE (γ_{sf}), unstable SFE (γ_{usf}), low index surface energies (γ_{111}, γ_{110}, γ_{100}), sublimation energy (E_{sub}) and single vacancy formation energy (E_{vac}).

The anharmonicity of a crystal is guaranteed if its cohesive energy *versus* lattice constant curve satisfies Rose's equation, namely the so-called universal state equation of metals (Fig. 3(d)) (Rose et al., 1984):
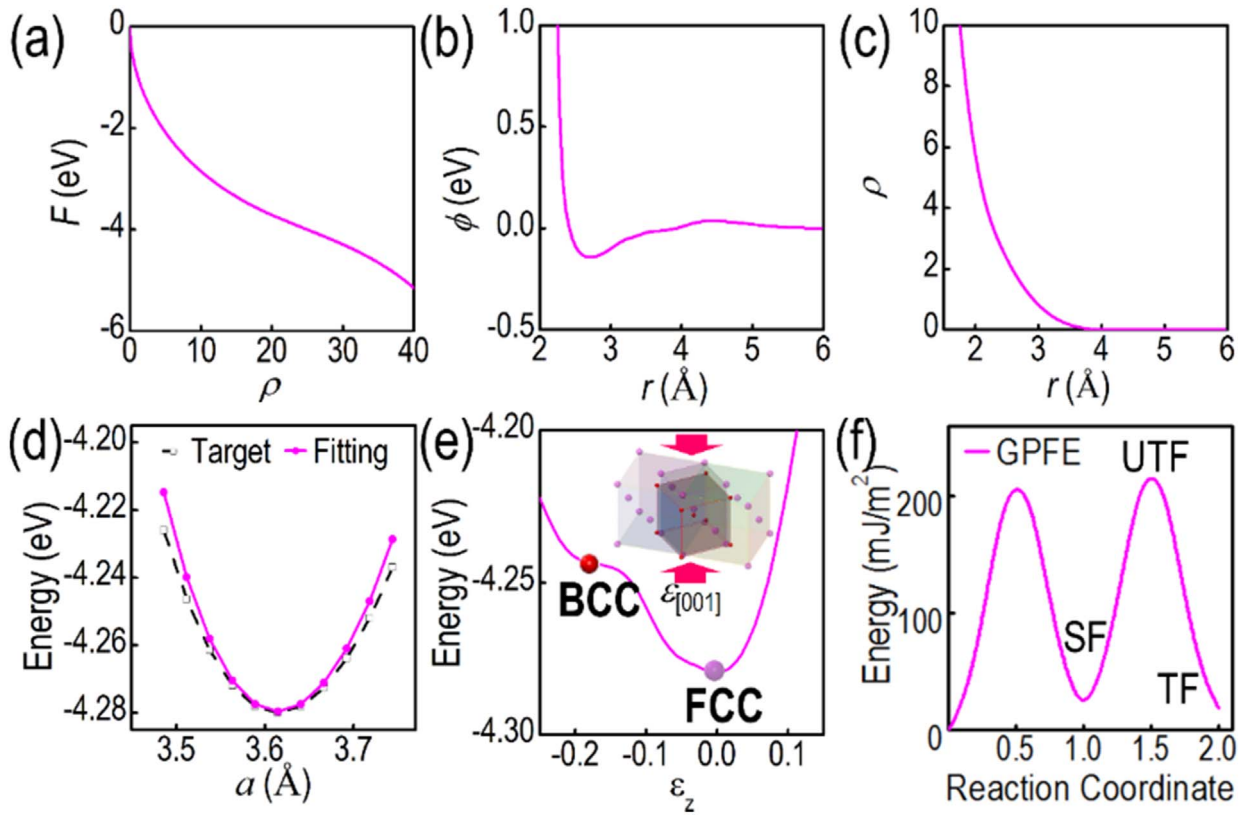
Fig. 3. Meta atom potential for a TWIP steel with composition of Fe-22 wt%Mn. (a) The embedding functions $F(\rho)$, (b) the pair interaction functions $\phi(r)$ and (c) the electron density function $\rho(r)$. (d) Fitting to Rose's equation. (e) The energy landscape of Bain's transformation (inset) that connects FCC and body-centered-cubic configurations. (f) The corresponding generalized planar fault (GPF) energy for the stacking and twin fault planar defects. The GPF curve for a SF is obtained by rigidly shearing a perfect crystal along < 112 > on a (111) plane, and the GPF curve for a twin fault (TF) is obtained by rigidly shearing a perfect crystal containing a pre-existing SF.

$$E(r_{\text{WS}}) = E_{\text{sub}} \cdot (-1 - a^* - 0.05a^{*3}) \cdot e^{-a^*} \tag{4}$$

where $a^* \equiv (r_{\text{WS}} - r_{\text{WSE}})/l$ and $l \equiv \sqrt{\frac{E_{\text{sub}}}{12\pi B r_{\text{WSE}}}}$, and r_{WS}, r_{WSE} and B denote, respectively, the radius of the Wigner-Seitz sphere containing an average volume per atom, the equilibrium Wigner-Seitz radius and the isothermal bulk modulus. The route of Bain's transformation (Bain, 1924; Milstein et al., 1994; Weixue and Tzuchiang, 1998), accounting for structural transformation with minimal atomic motion, is also considered in the optimization scheme in order to retain the stability of the lattice structure (Fig. 3(e)). The difference in free energies and the phase transformation barrier are both adopted as fitting parameters in order to ensure structural stability. Meanwhile, the propensity transformation from FCC to HCP structures can be suppressed by prescribing a transformation enthalpy of $\Delta H^{\text{fcc}\rightarrow\text{hcp}}$=3.82 meV. The < 112 > -direction slips on {111} planes, as an essential mechanism for the buildup of complex deformation-induced microstructures, are primarily governed by the carved generalized planar fault energy

Table 1
Fitting parameters of the meta atom potential for TWIP steel.

Material property	Target value	Meta-atom TWIP steel
a (fcc) (Å)	3.615 (Pierce, 2012)	3.614
E_{coh} (eV/atom)	−4.28 (Chamati et al., 2006)	−4.28
C_{11} (GPa)	175 (Pierce, 2012)	179
C_{12} (GPa)	83 (Pierce, 2012)	101
C_{44} (GPa)	97 (Pierce, 2012)	108
E_{vac} (eV)	1.7 (Kim and Buyers, 1978)	1.69
γ_{111} (mJ/m^2)	1900 (J.P. Hirth, 1982)	927
γ_{110} (mJ/m^2)	2100 (J.P. Hirth, 1982)	1308
γ_{100} (mJ/m^2)	2000 (J.P. Hirth, 1982)	1054
γ_{sf} (mJ/m^2)	19 (Allain et al., 2004)	19
γ_{usf} (mJ/m^2)	200 (Medvedeva et al., 2014)	211

P. Wang et al.

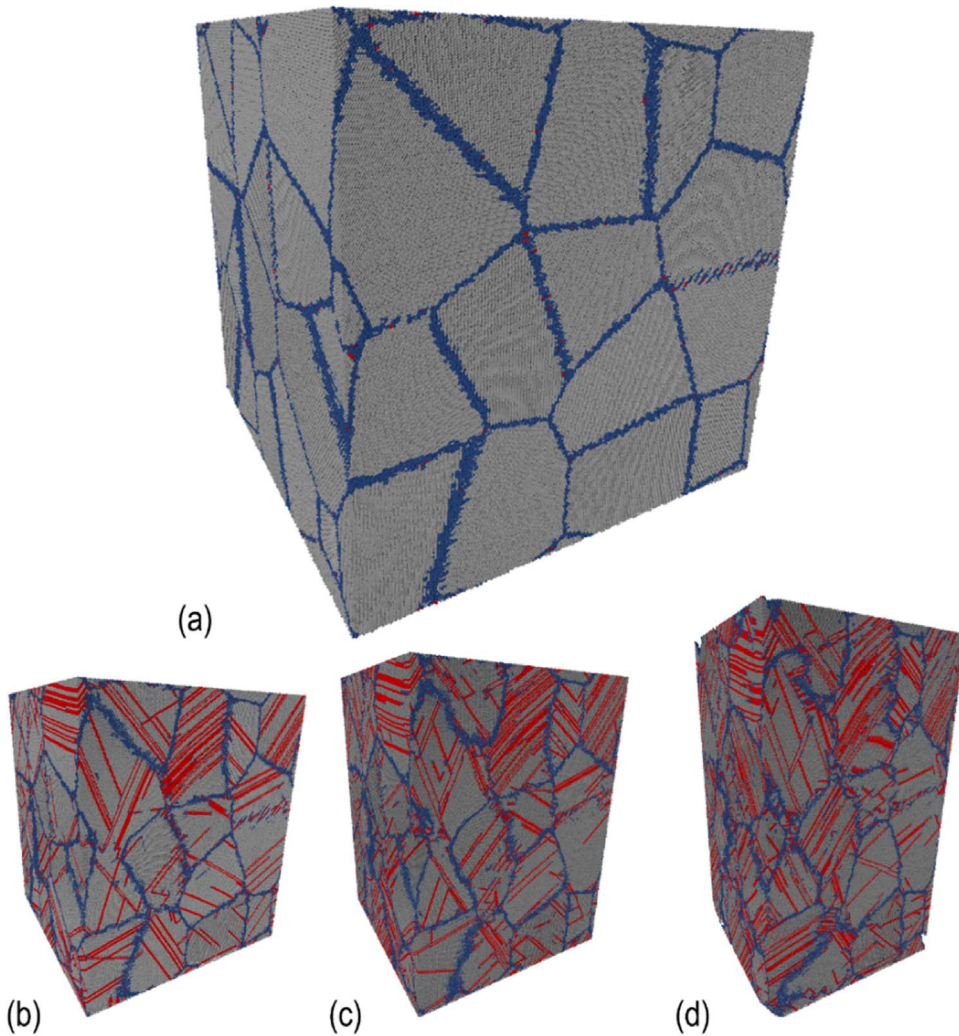J. Mech. Phys. Solids 98 (2017) 290–308

Fig. 4. Uniaxial deformation of a three-dimensional sample of polycrystalline TWIP steel with an average grain size 20 nm at different engineering strains: (a) 0%, (b) 10%, (c) 20% and (d) 40%. Color scheme: Gray: FCC atom; Red: HCP atom; blue: unknown atom. (For interpretation of the references to color in this figure legend, the reader is referred to the web version of this article.)

curve (Fig. 3(f)), which quantifies the energy change along the slipping path. The parameters γ_{sf} and γ_{usf} determine the shape of the GPF curve. They are rather sensitive to alloy composition and critical fitting parameters for the TWIP steel potential.

3.2. Simulation details

The open source MD code of Large-scale Atomic/Molecular Massively Parallel Simulator (LAMMPS) (Plimpton, 1995) was used for the simulations of fully three-dimensional polycrystal samples (Fig. 4). The samples were constructed using the Voronoi algorithm with 27 randomly oriented grains. The samples with an average grain size of 20 nm have dimensions of $60 \times 60 \times 60$ nm^3, and contain 18,200,000 atoms. Periodic boundary conditions were imposed in all three directions. All simulations were performed at the temperature of 300 K, with a fixed time step of 1 fs and a Nosé-Hoover thermostat. Before the uniaxial loading, the samples were fully relaxed for 100 ps. During loading, a 60% strain was applied at a constant strain rate of 2×10^8 s^{-1}.

In order to visualize the twin evolution in simulations, we modify the traditional coloring scheme of common neighbor analysis (CNA) (Faken and Jónsson, 1994). The atoms are initially classified by the CNA method into three groups, namely face-centered cubic (FCC), hexagonal close packed (HCP) and non-structured atoms. For each HCP atom, if the number of its nearest neighbor HCP atoms ($r_c = \sqrt{2}/2a$) is between 5 and 7 and larger than 5, that atom is labeled as a twin atom. In our text, the FCC, HCP, twin and non-structured atom are colored in white, orange, purple and green, respectively. Apparently, the twin boundary (TB) could be identified from the stacking fault or other defects in FCC lattice using this modified coloring scheme.
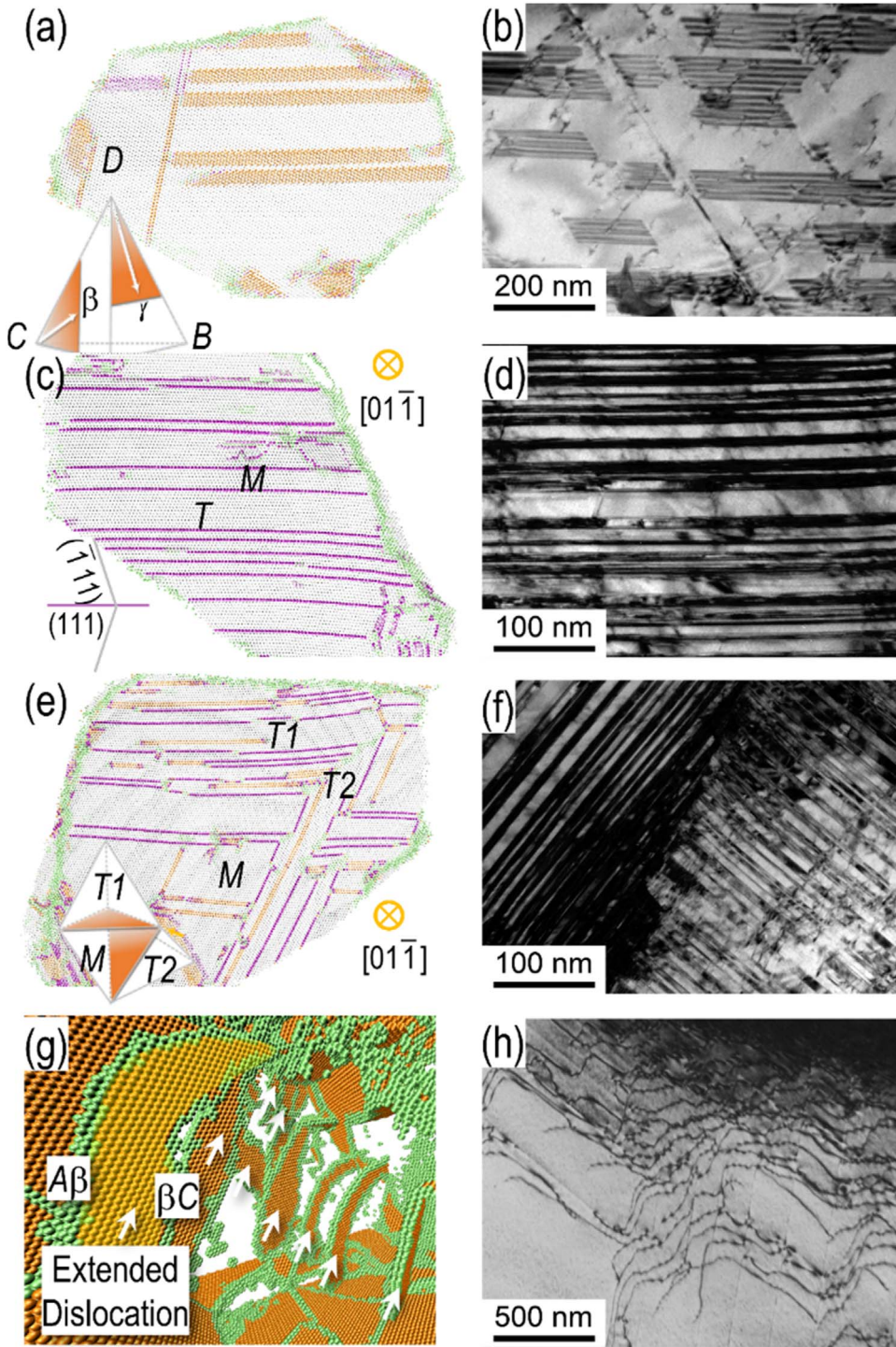
Fig. 5. Comparison of typical deformation-induced microstructures by MAMD simulations and TEM observation at different deformation stages. (a–b) Long SFs transecting a whole grain at strains less than 10%; (c–f) Formation of primary and secondary twin structures at medium to high strains (30–50%); (g–h) Abundant extended dislocations in both simulations and experiments. Insets to (a) and (e) are Thompson tetrahedrons, illustrating SF orientation and primary-secondary twin relation in FCC lattice, respectively. Color scheme: SF in orange; TB in purple; both partial dislocation and GB in green. (For interpretation of the references to color in this figure legend, the reader is referred to the web version of this article.)
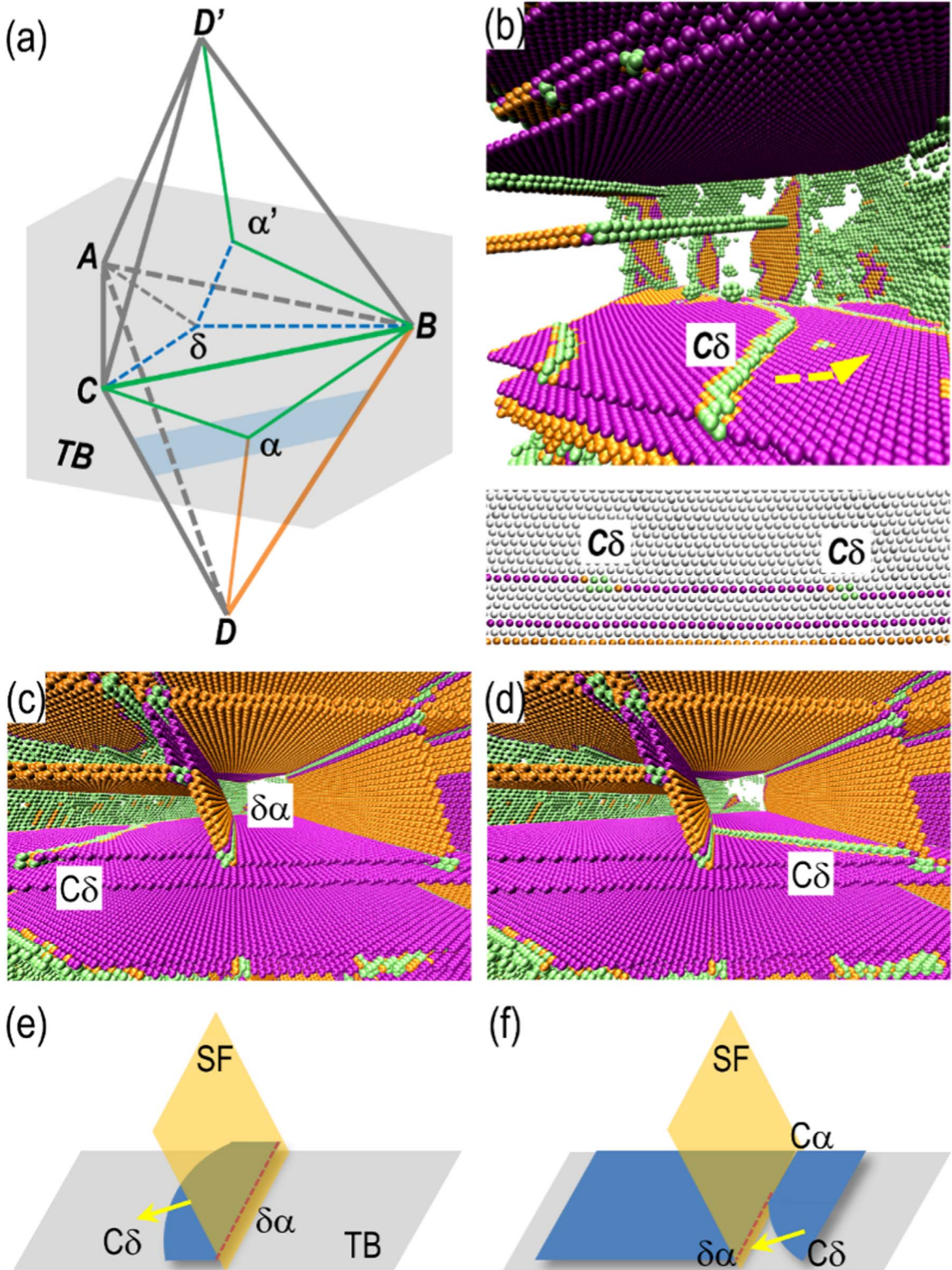
Fig. 6. Twin-slip interactions. (a) The double Thompson's tetrahedron with δ plane as the coherent TB. Unless specified otherwise, all the matrix dislocations are considered to slip in α plane and the twinning partials glide in δ or δ′ plane. (b) A deformation twin grows layer-by-layer with the successive emission of Cδ on adjacent slip planes from a GB. (c) A partial dislocation nucleates at and propagates from the intersection between SF and TB. (d) Sweeping of the GB-nucleated partial dislocation removes the stair-rod dislocation. (e–f) Schematical showings for the corresponding processes in (c) and (d).

4. Stacking faults in TWIP steels

4.1. A comparison study of microstructure evolution by simulation and TEM observation

A number of MD simulations have been carried out on deformation twinning in metals or alloys with low SFE, which is known to be crucial for the remarkable high work hardening rates observed in experimental studies (Choi et al., 2015; Christian and Mahajan, 1995; Gutierrez-Urrutia and Raabe, 2012; Steinmetz et al., 2013; Zhu et al., 2012). Here, we have performed MAMD simulations on fully three-dimensional polycrystals with an average grain size of 20 nm (Fig. 4). At the initial stage, the plastic deformation is mainly carried by the gliding of partial dislocations nucleated from the grain boundaries. The associated SFs either transect the whole grain or are stopped by the other inclined SFs (Fig. 5(a)), as consistent with the typical TEM observation shown in Fig. 5(b). Deformation twinning is frequently observed at larger plastic strains (Fig. 5(c–e)). The primary twin structures are formed in grains with one dominant slip system being activated (Fig. 5(c)). Due to the random texture, competition among various slip systems leads to multiple deformation twin variants (Fig. 5(e)). These microstructures match well with our TEM images on severely deformed TWIP steels (Fig. 5(d) and (f)), as well as with those in the literature (Choi et al., 2015; Gutierrez-Urrutia and Raabe, 2012; Steinmetz et al., 2013). It is noted that a high density of extended dislocations also serves as important carriers of plastic deformation in the TWIP steel, as revealed by both MAMD simulations (Fig. 5(g)) and experiments (Fig. 5(h)). So far, the mechanical behaviors of low SFE alloys as determined by the dynamic interactions among these typical microstructures have been investigated largely from theoretical viewpoints and experimental evidences (Choi et al., 2015; Gutierrez-Urrutia et al., 2010; Shen et al., 2015; Steinmetz et al., 2013). The fact that our MAMD simulations consist with the existing studies provides a validation of the proposed meta-atom method.

4.2. Interactions between twinning and gliding dislocations at twin boundaries

As observed in both experiments and MAMD simulations, the deformation twinning process is mainly carried by slips of perfect and partial dislocations. Interactions between twinning and gliding dislocations at TBs are believed to make twinning an effective strategy in simultaneously increasing strength and ductility of TWIP steels (Steinmetz et al., 2013). To classify the twin-slip and twin-dislocation interactions in simulations, we adopt a double tetrahedron notation proposed by Hartley and Blachon (Fig. 6(a)) (Hartley and Blachon, 1978). The following interactions are enumerated below.
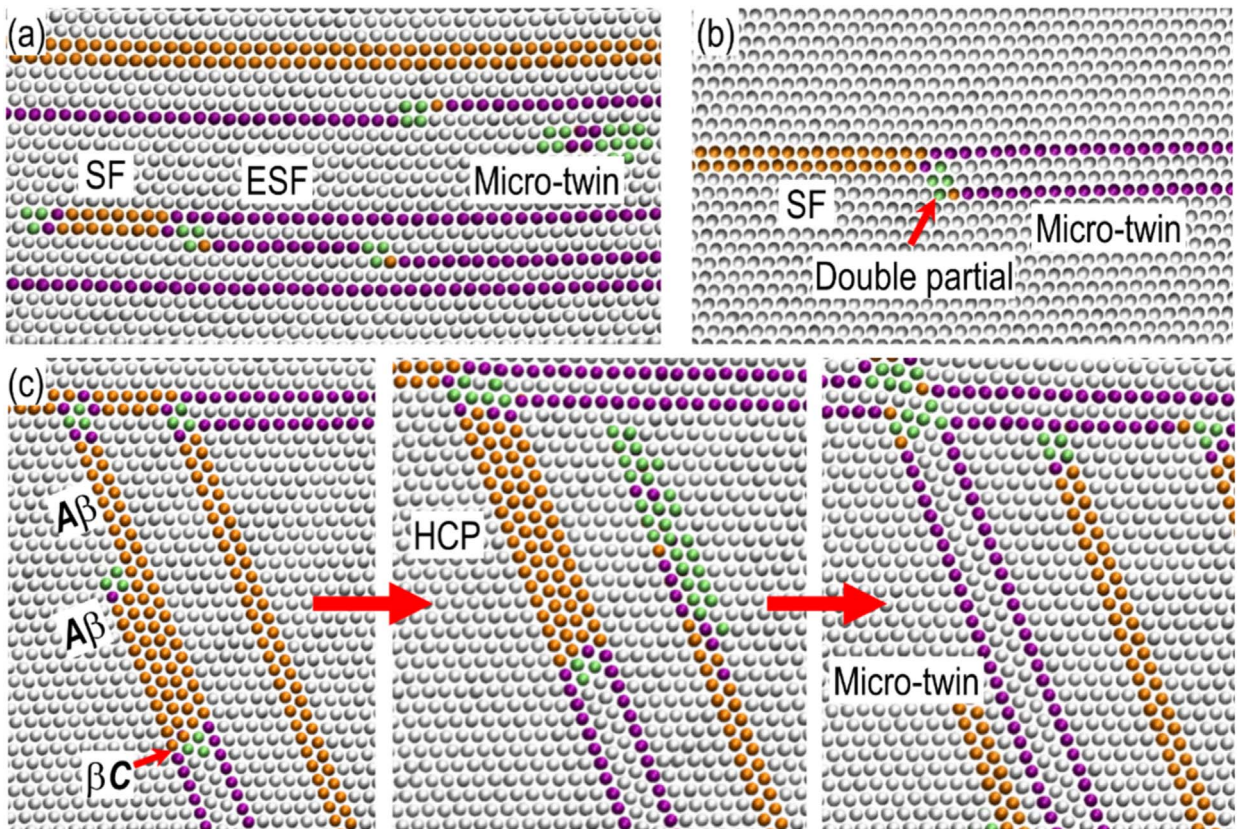

Fig. 7. Typical twin nucleation mechanisms. (a) Micro-twin is formed by successive emissions of Shockley partials from the grain boundary on the right. (b) Double Shockley partials. (c) Transformation of a four-layer HCP phase into a twin lamella.
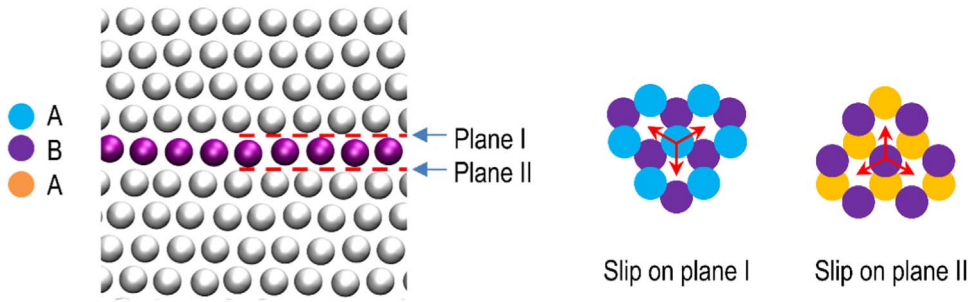
Fig. 8. Permissible slips right above or below a TB. The slip planes are denoted as plane I and plane II. Clearly, the slipping directions on plane I are opposite to those on plane II.
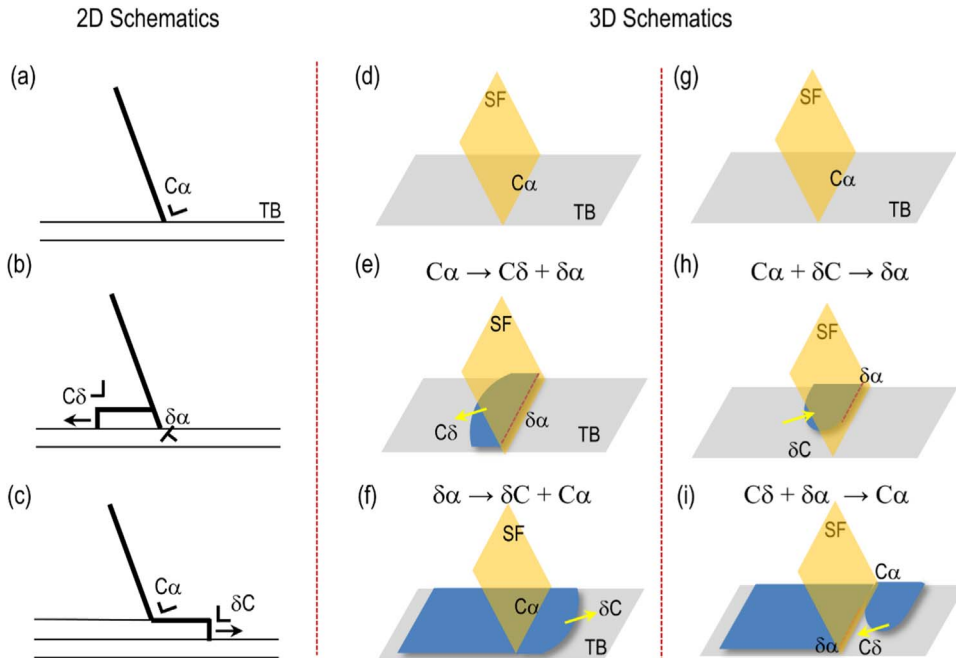

Fig. 9. Representations of twin-slip interactions at a TB in two-dimensional and three-dimensional views. (a–c) Dislocation reactions lead to migration of the TB by one layer in a two-dimensional schematic. (d–f) The realization of (a–c) by dislocation dissociation. (g–i) The realization of (a–c) by dislocation combination. Both (d–f) and (g–i) give the same two-dimensional sketch, but they correspond to different mechanisms.

(1) **Cδ**. Gliding of Shockley partials (*e.g. Cδ*) along TBs (δ), the so-called twinning partials, contributes significantly to the nucleation and growth of deformation twins, as well as to the detwinning process. Fig. 6(b) shows a twin lamella formed by repetitive emission of twinning partials from GBs onto successive (111) stacking planes, according to a layer-by-layer growth mode. Other nucleation mechanisms are presented in Fig. 7. A three-layer twin embryo can be nucleated at GBs by emitting a group of three twinning partials on adjacent planes (Fig. 7(a)) (Mahajan and Chin, 1973; Steinmetz et al., 2013), which are of the same type and remain separated. Double Shockley partials, as proposed by Hirth and Hoagland (Hirth and Hoagland, 1998), can be formed by combining two partials with different Burgers vectors on neighboring glide planes (Fig. 7(b)). Occasionally, two intrinsic stacking faults (ISF) overlap and transform local FCC lattice into an unstable four-layer HCP phase (Fig. 7(c)). The inner two HCP planes, one from each of the two ISFs, are quickly transformed back to FCC planes *via* gliding of a twinning partial, leaving a four-layer twin lamella. This energetically driven process has been naturally incorporated in the meta-atom potential by design. It is noted that GB networks are prolific partial dislocation sources in low-SFE metals (Li et al., 2010, 2009; Van Swygenhoven, 2002; Van Swygenhoven et al., 2004a, 1999; Yamakov et al., 2002, 2004), as observed in our simulations. Movie S1 reveals a high mobility TB migration process assisted by a flooding of GB-nucleated twinning partials, regardless the high-density of defects stored in the TBs. As a consequence, this mechanism dominates twin formation and TB migration, which accounts for a significant fraction of the total plastic strain.

Supplementary material related to this article can be found online at http://dx.doi.org/10.1016/j.jmps.2016.09.008.

$$C\alpha \rightarrow C\delta + \delta\alpha \tag{5}$$
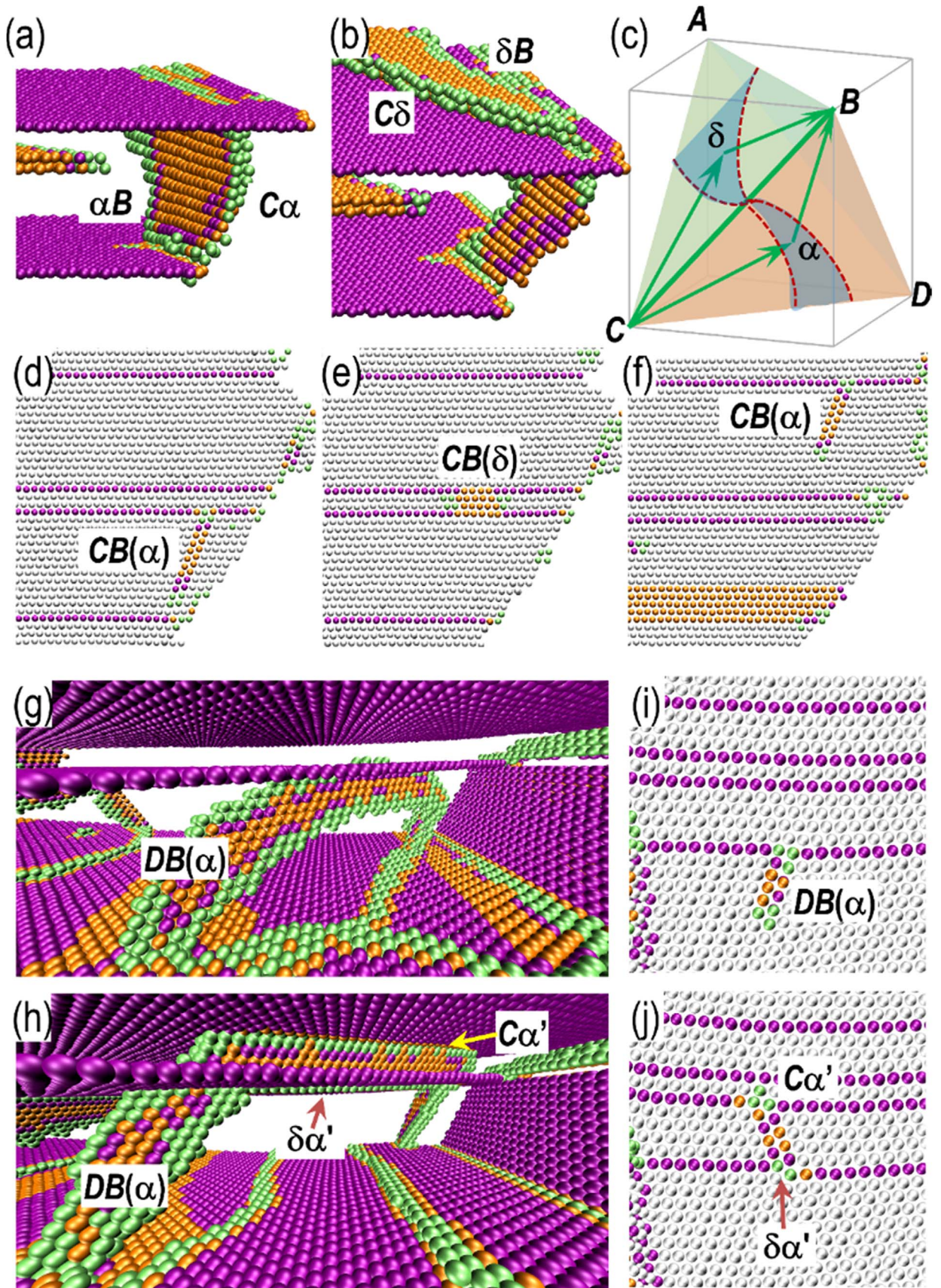
where δα corresponds to a net stair-rod dislocation. This process is not spontaneous and only observed occasionally in our simulations (Fig. 6(c)). The twinning partial (Cδ) associated with the dissociation of a 30° Shockley partial (*e.g.* Cα) accorwding to (5) can only glide along one of the permissible slipping directions. The latters are opposite for planes I and II shown in Fig. 8. Slipping on plane I (or II) increases (or decreases) the twin thickness by one layer and, consequently, undergoes a different energy change under a given local stress state. Therefore, only certain 30° Shockley partials can react with TBs according to (5).

It is also found that a TB can retain a high migration mobility even when intersected by a high-density of SFs (Movie S1). Here, the most frequently observed dislocation reactions are

$$C\alpha + \delta C \rightarrow \delta \alpha \tag{6}$$

$$C\delta + \delta \alpha \rightarrow C\alpha \tag{7}$$
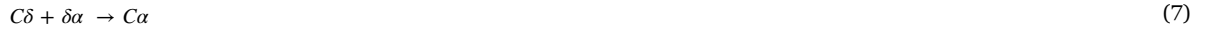
Reaction (6) gives similar observation as reaction (5), and is easily confused with, the latter especially in a two-dimensional view (Fig. 9). Unlike (5), reaction (6) takes place spontaneously. A stair-rod dislocation (δα), appearing as an atomic step at the intersection, can be removed following reaction (7), which is also spontaneous. Sketches of the above reactions are shown in Fig. 8(e−f) and Fig. 9. Assisted by prolific GB dislocation sources, repeating reactions (6) and (7) in sequence leads to fast migration of TBs, as observed in Movie S1. Reaction (6) serves as an elementary mechanism in forming more complex twin structures, different from reaction (5) reported in the early works (Christian and Mahajan, 1995; Zhu et al., 2012, 2009, 2011).

(4) **CB(α)**. If the requirements for reaction (6) is not satisfied, a trailing Shockley partial (αB) can be partly driven close to the leading partial (Cα), forming an extended screw dislocation segment (Cα+αB→CB(α)) (Fig. 10(a,b)). Constriction and re-dissociation onto the twinning plane facilitate a cross-slip process (CB(δ)→Cδ+δB) and create a local constricted node connecting CB(δ) and CB(α). A complete cross-slip is finished by a step-by-step fast movement of the node, significantly lowering the energy barrier. Fig. 10(c) schematically shows the corresponding process. For a twin lamella with four-layer thickness, the extended dislocation CB(δ) is in contact with both TBs. Another cross-slip from δ to α' will make CB(α) completely transmitted through the twin, leaving TBs intact (Fig. 10(d−f). Sequential cross slips are required to realize transmission in a thicker twin, which is rarely observed. For most of the time, extended dislocations are trapped inside twins, increasing the stored defect density.

(5) **DB(α)**. The 90° Shockley partials (Dα) are effectively blocked by TBs. Combining with a trailing partial dislocation (*e.g.* αB), it can transect the twin on α' plane with Burgers vector Cα' and leaves a stair-rod dislocation (δα') on the TB (Fig. 10(g,h)). The dislocation reaction can be written as

$$DB(\alpha) \rightarrow C\alpha' + \delta\alpha' \tag{8}$$

It is noted that this reaction lowers the total energy and transforms a 90° Shockley partial (Dα) into a 30° Shockley partial (Cα'), signifying the importance of reactions (6) and (7). The corresponding 2D views are shown in Fig. 10(i-−j).

4.3. Tubular structure formation due to stacking interactions

A high-density of forest extended dislocations (Fig. 5(g−h) and Fig. 11) is another important feature of cold-worked TWIP steels. Constricted dislocation jogs are formed by transecting these dislocations with SFs (Fig. 11(a,b)). A super jog can be observed at the intersection between a twin lamella and an extended dislocation (Fig. 11(d,e)). Non-conservative jog motion produces vacancies (v) either individually or in the form of tubes (Fig. 11(c) and (f)), which has been extensively studied in Cu (Hirsch, 1962; Vegge et al., 2001; Zhou et al., 1998, 1999).

Our simulations reveal that similar vacancy tubes are more easily formed in TWIP steels (Fig. 12), which is characterized by SF interactions especially at the early deformation stage. We propose an opposite double tetrahedron notation (Fig. 12(g)) to classify the observed SF interactions with the assumption that a SF is already present along the α (or α') plane, denoted as SF(α). The incident leading and trailing Shockley partials slip on δ (or δ') plane, are marked with symbols ∧ and ∨, respectively. Penetration by a 90° Shockley partial, with a Burgers vector of $\widehat{A\delta}$ or $\widecheck{\delta A}$, will geometrically generate a vacancy (v) or interstitial (i) tube, respectively. The associated high energy barrier makes single SF(α) an effective obstacle to slip. For a 30° Shockley partial (*e.g.* $\widecheck{\delta C}$), a stair-rod dipole δα-δ'α' forms at the intersection, as indicated in Fig. 12(d) and (g). It is noted that the slip vector δC is equal to δ'B on the right side of the α plane in this opposite double tetrahedron setup (Fig. 12(g)). Two Frank dislocations with opposite directions are sequentially generated according to A'δ'+δ'α→A'α' (Fig. 12(b) and (e)) and Aδ+δα→ Aα (Fig. 12(c) and (f)). A vacancy tube is formed by annihilating Aα and A'α' located on the neighboring planes. Such tubes may provide fast diffusion channels for small

Fig. 10. Twin interactions with extended dislocations. (a) Intersection between a TB and an extended dislocation CB(α). (b) Cross-slip of CB(α) onto δ plane. (c) Representation of the cross-slip using Thompson's tetrahedron. (d−f) Transmission of a screw dislocation through a four-layer twin lamella in a sequence of cross-slip processes. (g−h) Cross slip of an extended dislocation with edge component. The corresponding 2D views are shown in (i−j), respectively.
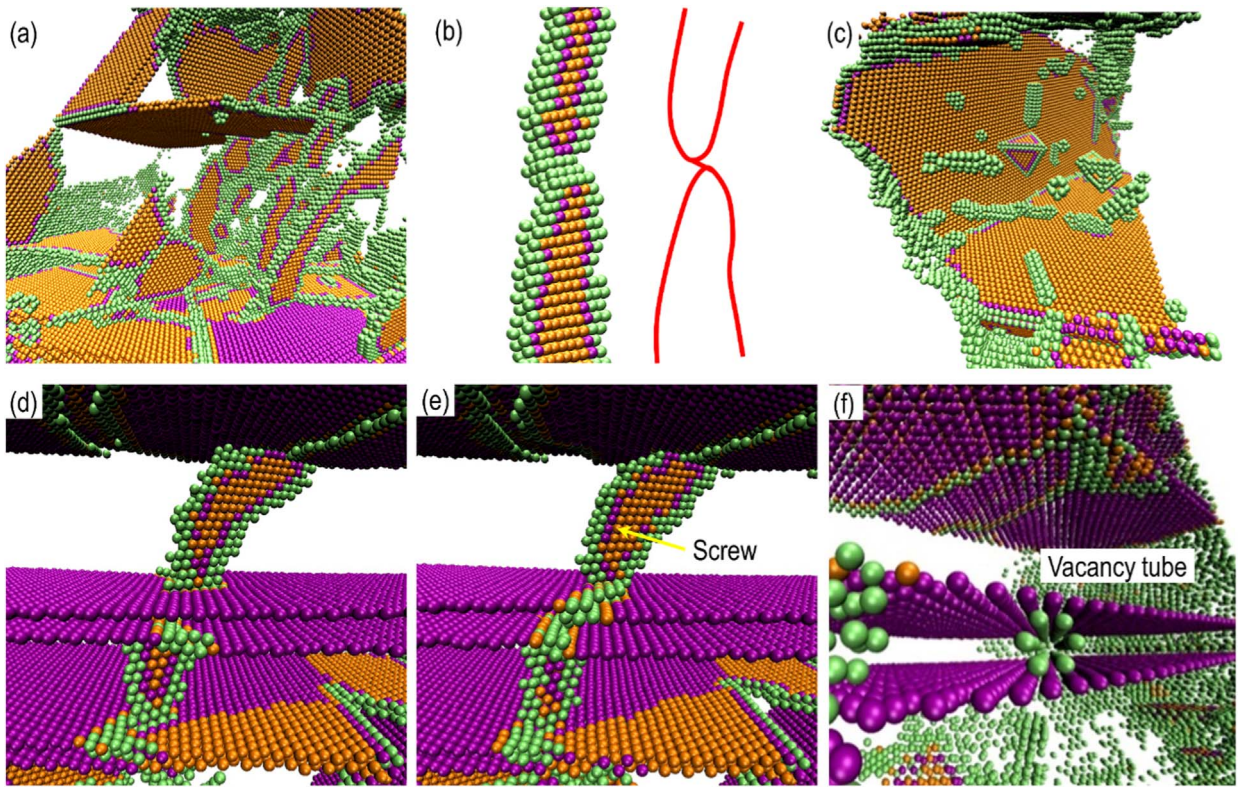
Fig. 11. Vacancies created by non-conservative motion of dislocation jogs. (a) Extended dislocation forests with jogs. (b) One extended dislocation with a constricted jog. (c) Vacancies created by non-conservative motion of dislocation jogs. (d-e) A super jog is formed by sectioning a screw dislocation with a twin lamella. (f) Vacancy tube is formed after the super jog moves away.
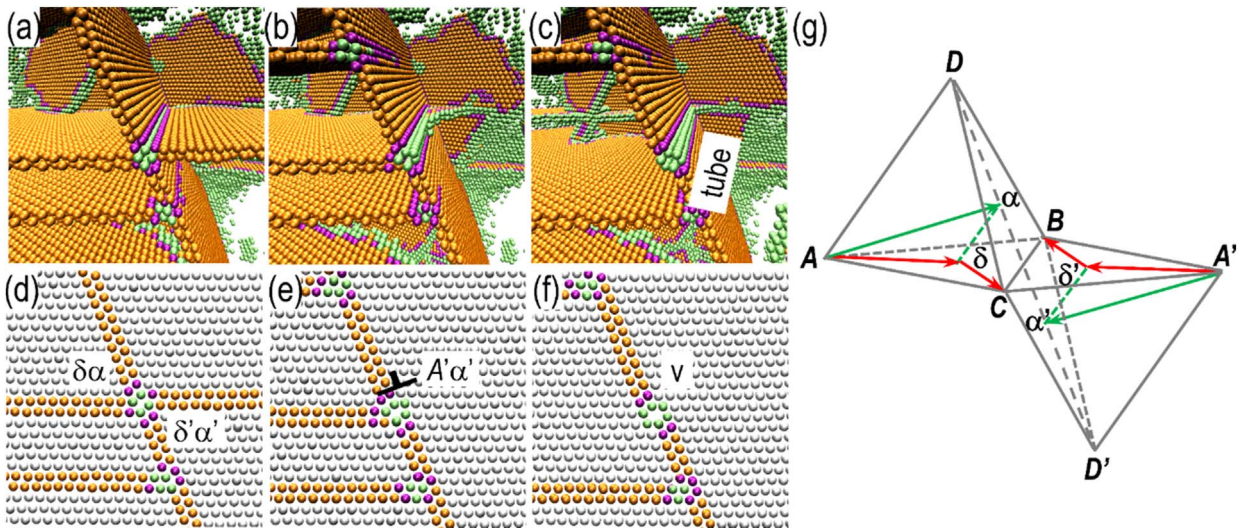
Fig. 12. A vacancy tube formation mechanism by SF interactions. (a) Intersection of two SFs and dislocation reactions (b–c) lead to the formation of a vacancy tube. The corresponding 2D views are shown in (d–f), respectively. (g) Opposite double tetrahedron notation.

solute atoms, such as C, N, Si or Al in steels. It is expected that more pronounced bake hardening effect may take place in low-SFE alloys than in high-SFE ones at the early deformation stage. The leading and trailing slips shift the SF(α) by a vector AC (or A′B). Geometrically, reversing the slip vectors will create a line of interstitials, which is not observed in our simulations. If Bδ is the trailing Shockley partial, the stair-rod dipole will be erased and the lattice recovered to the original state (o). The SF interactions are

Fig. 13. Deformation twinning leads to partition of grains. (a) Intersection of SFs with TBs from both sides. (b) Secondary twin lamellae nucleate upon intensive slip of slanted partial dislocations. (c) Intersection between primary and secondary twins, as circled in (b), consists of an array of stair-rod dislocations. (d) Three-dimensional view of the stair-rod array.

summarized in (9)–(11).

$$\overset{\smallsmile}{A\delta} + \widehat{\delta C} \xrightarrow{\text{SF}(\alpha)} \text{v} \tag{9}$$

$$\overset{\smallsmile}{\delta A} + \widehat{C\delta} \xrightarrow{\text{SF}(\alpha)} \text{i} \tag{10}$$

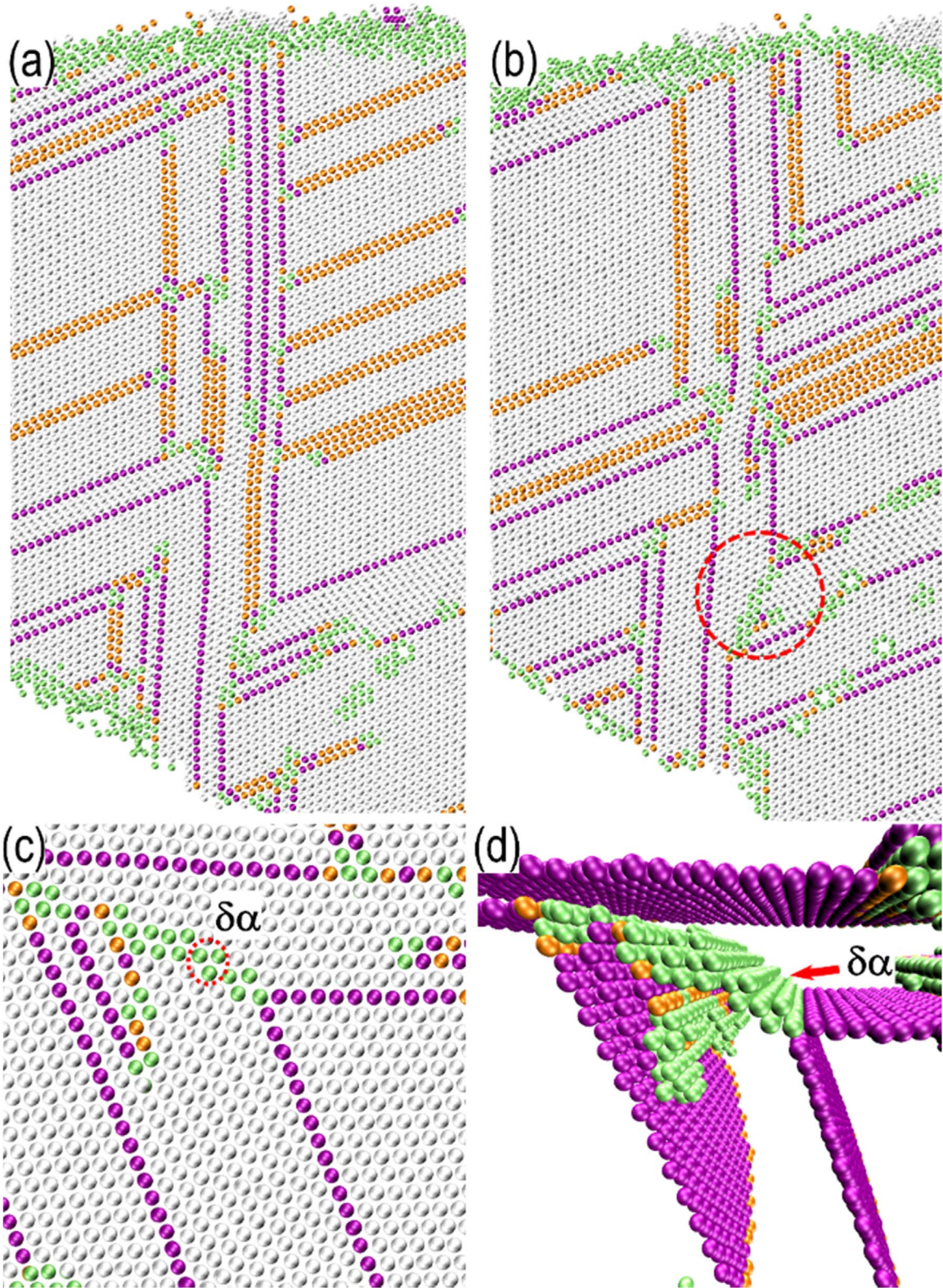$$B\delta + \delta C \xrightarrow{\text{SF}(\alpha)} \text{o} \tag{11}$$

4.4. Formation of multiple twin structure leads to grain refinement

Deformation twinning leads to dynamic grain refinement with TBs as effective barriers (Fig. 13(a,b)). The grain is separated into two parts by a transecting twin lamella. Multiple slanted partial dislocations impinge onto the TB, causing severe lattice distortion. The local strain is relaxed after nucleating a secondary twin embryo according to reactions (4) and (5). The V-shaped twin structure forms by nucleating a secondary twin separated from the primary twin by an array of stair-rod dislocations (Fig. 13(c,d) and Movie S2). The as-formed twin structures further partition the grain, which is expected to enhance the strength.

Supplementary material related to this article can be found online at http://dx.doi.org/10.1016/j.jmps.2016.09.008.

5. Competition among different stacking faults

In contrast to metals or alloys with medium to high SFEs, the deformation mechanism of TWIP steels, with SFE as low as 19 mJ m^{-2}, is mainly characterized by SF interactions, deformation twinning and intensive activities of extended dislocations. Whether the dislocation activity is dominated by extended partials or full dislocations strongly depends on the ratio of γ_{sf} to γ_{usf}, both are critical fitting parameters in optimizing the meta-atom potential. Similarly, the twinning propensity *via* gliding Shockley partials on adjacent planes is dependent on the ratio of γ_{utf} to γ_{usf}.

To the first order approximation, the variation of embedded energy during slipping can be neglected, and γ_{sf}, γ_{utf} and γ_{usf} can be calculated in the same form as

$$\gamma = \left(\frac{1}{2} \sum_m N_m \phi(\alpha_m \cdot a_0) \right) / S \tag{12}$$

where subscript m denotes the mth nearest neighbors, S is the projected area of one atom on a close-packed plane, and N_m and α_m are the number of the mth nearest neighbors and the corresponding geometric factor, respectively. We note that the values of N_m are different for the stacking, unstable stacking and unstable twinning configurations, while the values of α_m are identical for all configurations. Their values are given in Table 2. Clearly, for arbitrary m,

$$N_m(utf) = N_m(usf) + \tfrac{1}{2} N_m(sf) \tag{13}$$

Table 2
Geometric factors and number of mth nearest neighbors for calculating γ_{sf}, γ_{utf} and γ_{usf}.

Atomic shell	α_m	N_m (sf)	N_m (usf)	N_m (utf)
1	$\sqrt{11/24}$	0	4	4
2	$\sqrt{1/2}$	0	−6	−6
3	$\sqrt{17/24}$	0	4	4
4	1	0	−6	−6
5	$\sqrt{29/24}$	0	8	8
6	$\sqrt{4/3}$	4	0	2
7	$\sqrt{11/8}$	0	4	4
8	$\sqrt{35/24}$	0	4	4
9	$\sqrt{3/2}$	−12	−24	−30
10	$\sqrt{13/8}$	0	8	8
11	$\sqrt{11/6}$	24	0	12
12	$\sqrt{15/8}$	0	8	8
13	$\sqrt{47/24}$	0	8	8
14	$\sqrt{2}$	−12	−12	−18
15	$\sqrt{17/8}$	0	8	8
16	$\sqrt{19/8}$	0	4	4
17	$\sqrt{5/2}$	−24	−36	−48
18	$\sqrt{21/8}$	0	8	8
19	$\sqrt{65/24}$	0	8	8

Table 3
First principle calculations for γ_{sf}, γ_{utf} and γ_{usf}.

Potential	γ_{sf} (mJ m^{-2})	γ_{usf} (mJ m^{-2})	γ_{utf} (mJ m^{-2})	γ_{usf} + ½ γ_{sf} (mJ m^{-2})	Relative error[a]
Ag (Kibey et al., 2007)	18	133	143	142	−0.70%
Au (Kibey et al., 2007)	33	134	148	150.5	1.69%
Cu (Kibey et al., 2007)	41	180	200	200.5	0.25%
Ni (Kibey et al., 2007)	110	273	324	328	1.23%
Pd (Kibey et al., 2007)	168	287	361	371	2.77%
Pt (Kibey et al., 2007)	324	339	486	501	3.09%
Al (Kibey et al., 2007)	130	162	216	227	5.09%
Cu-5 at%Al (Kibey et al., 2006)	20	170	179	180	0.56%
Cu-8.3 at%Al (Kibey et al., 2006)	7	169	176	172.5	−1.99%

[a] Relative error is calculated as $[(\gamma_{usf}+½\,\gamma_{sf})-\gamma_{utf}]\,/\gamma_{utf}\times100\%$.

which directly leads to

$$\gamma_{utf} \approx \gamma_{usf} + \frac{1}{2}\gamma_{sf} \tag{14}$$

Surprisingly, this estimation gives good predictions for γ_{utf}, as verified by the available data based on first principle (Table 3), tight bonding (Table 4) and MD (Table 5) calculations.

According to (14), the energy barriers are always in the order of $\gamma_{usf} > \gamma_{utf}-\gamma_{sf} > \gamma_{usf}-\gamma_{sf}$ for FCC metals in generating a single SF, a twinning partial and a trailing partial dislocation, respectively. Since slip process is generally thermally activated in deforming alloys, the probability of relative occurrence for different mechanisms is exponentially proportional to the difference in barrier heights (γ_{sf} or ½ γ_{sf}). This leads to the conclusion that emission of a trailing partial dislocation is energetically more favorable than the nucleation of a deformation twin. However, a small γ_{sf} (*e.g.* 19 mJm^{-2} for the TWIP steel under consideration) greatly promotes deformation twining, as revealed by our simulations. The complex twin-slip and twin-dislocation interactions demonstrate the dual role of deformation twins as barriers or storages of dislocations, potentially contributing to the high strength and ductility of TWIP steels.

6. Summary

A meta atom method has been proposed to unify MD simulations of both pure metals and alloys in the framework of EAM potentials. The universality of the EAM potential provides adequate flexibility in constructing model materials with properties varying in a large range, covering spectra of different classes of metallic alloys. In this paper, we have developed a meta-atom potential for a TWIP steel with SFE as low as 19 mJm^{-2}. Fully three-dimensional MD simulations reveal that interactions between slipping and deformation twinning can account for most of the microstructural evolutions observed in experiments. It is found that a TB can retain high migration mobility even when intersected by a high-density of SFs due to the assistance of spontaneous dislocation reactions. This process serves as the intrinsic mechanism in forming complex twin structures. Deformation twinning leads to dynamic grain refinement with TBs as effective barriers, and consequently enhances the strength. Our simulations also reveal that vacancy tubes are more easily formed in TWIP steels due to SF interactions especially at the early deformation stage, which is special for metals with low SFEs. The complex twin-slip and twin-dislocation interactions demonstrate the dual role of deformation twins as both barriers and storages of dislocations, potentially contributing to the high strength and ductility of TWIP steels.

Accordingly, the macroscopic measurable quantities can be incorporated into the meta-atom potentials for engineering alloys, so that massively parallel MAMD simulations can be enabled to shed light on the microscopic deformation mechanisms and to facilitate the construction of materials with specific mechanical properties. Finally, based on the meta-atom method, it is shown that $\gamma_{utf} \approx \gamma_{usf} + \frac{1}{2}\gamma_{sf}$, which highlights the uniqueness of γ_{sf} in determining competition among the processes of generating a single SF, a

Table 4
Calculated values of γ_{sf}, γ_{utf} and γ_{usf} by tight-bonding method.

Potential	γ_{sf} (mJ m^{-2})	γ_{usf} (mJ m^{-2})	γ_{utf} (mJ m^{-2})	γ_{usf}+½ γ_{sf} (mJm^{-2})	Relative error
Ag (Bernstein and Tadmor, 2004)	18	93	105	102	−2.86%
Al (Bernstein and Tadmor, 2004)	99	164	207	213.5	3.14%
Au (Bernstein and Tadmor, 2004)	49	110	135	134.5	−0.37%
Cu (Bernstein and Tadmor, 2004)	64	200	236	232	−1.69%
Ir (Bernstein and Tadmor, 2004)	305	679	872	831.5	−4.64%
Pb (Bernstein and Tadmor, 2004)	30	98	108	113	4.63%
Pd (Bernstein and Tadmor, 2004)	107	313	355	366.5	3.24%
Pt (Bernstein and Tadmor, 2004)	270	388	521	523	0.38%

Table 5
Calculated values of γ_{sf}, γ_{utf} and γ_{usf} by MD simulations.

Potential	γ_{sf} (mJ m^{-2})	γ_{usf} (mJ m^{-2})	γ_{utf} (mJ m^{-2})	γ_{usf}+½ γ_{sf} (mJ m^{-2})	Relative error
Ni (Van Swygenhoven et al., 2004b)	304	551	704	703	−0.14%
Ni (Mishin et al., 1999)	120	172	234	232	−0.85%
Cu (Van Swygenhoven et al., 2004b)	21	154	163	164.5	0.92%
Cu (Van Swygenhoven et al., 2004b)	34	173	190	190	0.00%
Al (Mishin et al., 1999)	146	151	200	224	12.00%
Al (Ercolessi and Adams, 1994)	95	124	150	171.5	14.33%

twinning partial and a trailing partial dislocation. This approach may pave a practical way to understand the mechanical behaviors of complex alloys that takes the full advantage of the rapidly increasing computational power.

Acknowledgments

Appendix A

See Tables A1 and A2.

Table A1
Knots for the pair function.

No.	r_i (Å)
0	2
1	2.4
2	2.8
3	3.2
4	3.5
5	4
6	4.6
7	5.4
8	6

Table A2
Summary of the fitting coefficients.

	TWIP steel		TWIP steel
a_1	−9.500000000000000e-01	$c_{3,4}$	4.293559073390630e+00
a_2	1.618465111936526e-03	$c_{4,3}$	3.791895483309166e+00
a_3	−6.762905624654250e-07	$c_{4,4}$	−3.670595358210705e+00
b_0	−6.277114387582506e+00	$c_{5,3}$	1.899517741423221e-02
b_1	0	$c_{5,4}$	−1.222018433436698e+00
b_2	5.000000000000000e+01	$c_{6,3}$	−4.028413605605736e-01
$c_{1,3}$	7.410332271283292e+01	$c_{6,4}$	3.695323363306102e-01
$c_{1,4}$	6.848516616595713e+02	$c_{7,3}$	−4.338132774276135e-02
$c_{2,3}$	−2.163946029666258e+00	$c_{7,4}$	1.197693208633643e-02
$c_{2,4}$	7.924697619521995e+00	$c_{8,3}$	2.600124439135270e-02
$c_{3,3}$	3.949239092637880e+00	$c_{8,4}$	-5.584234894549544e-03

References

Ackland, G.J., Bacon, D.J., Calder, A.F., Harry, T., 1997. Computer simulation of point defect properties in dilute Fe—Cu alloy using a many-body interatomic potential. Philos. Mag. A 75, 713–732.

Allain, S., Chateau, J.P., Bouaziz, O., Migot, S., Guelton, N., 2004. Correlations between the calculated stacking fault energy and the plasticity mechanisms in Fe—Mn—C alloys. Mater. Sci. Eng. A 387–389, 158–162.

P. Wang et al.

J. Mech. Phys. Solids 98 (2017) 290–308

Ashby, M.F., 1972. A first report on deformation-mechanism maps. Acta Met. 20, 887–897.

Bain, E.C., 1924. The nature of martensite. Trans. Am. Inst. Min. Met. Eng. 70, 25–46.

Bernstein, N., Tadmor, E.B., 2004. Tight-binding calculations of stacking energies and twinnability in fcc metals. Phys. Rev. B 69, 094116.

Bragg, L., Nye, J.F., 1947. A Dynamical Model of a Crystal Structure.

Chamati, H., Papanicolaou, N.I., Mishin, Y., Papaconstantopoulos, D.A., 2006. Embedded-atom potential for Fe and its application to self-diffusion on Fe. Surf. Sci. 600, 1793–1803.

Choi, W.S., De Cooman, B.C., Sandlöbes, S., Raabe, D., 2015. Size and orientation effects in partial dislocation-mediated deformation of twinning-induced plasticity steel micro-pillars. Acta Mater. 98, 391–404.

Christian, J.W., Mahajan, S., 1995. Deformation twinning. Prog. Mater. Sci. 39, 1–157.

Cooman, B.C.D., Chin, K.-g., Kim, J., 2011. High Mn TWIP steels for automotive applications. In: Chiaberg, M. (Ed.), New Trends and Developments in Automotive System Engineering. InTech, Croatia.

Daw, M.S., Baskes, M.I., 1983. Semiempirical, quantum mechanical calculation of hydrogen embrittlement in metals. Phys. Rev. Lett. 50, 1285–1288.

Daw, M.S., Baskes, M.I., 1984. Embedded-atom method: derivation and application to impurities, surfaces, and other defects in metals. Phys. Rev. B 29, 6443–6453.

Daw, M.S., Foiles, S.M., Baskes, M.I., 1993. The embedded-atom method: a review of theory and applications. Mater. Sci. Eng. R 9, 251–310.

Ercolessi, F., Adams, J.B., 1994. Interatomic Potentials from First-Principles Calculations: the Force-Matching Method. EPL (Europhys. Lett.) 26, 583.

Faken, D., Jónsson, H., 1994. Systematic analysis of local atomic structure combined with 3D computer graphics. Comput. Mater. Sci. 2, 279–286.

Fan, Y., Osetskiy, Y.N., Yip, S., Yildiz, B., 2013. Mapping strain rate dependence of dislocation-defect interactions by atomistic simulations. Proc. Natl. Acad. Sci. USA 110, 17756–17761.

Finnis, M.W., Sinclair, J.E., 1984. A simple empirical n-body potential for transition-metals. Philos. Mag. A 50, 45–55.

Georges, J.M., Meille, G., Loubet, J.L., Tolen, A.M., 1986. Bubble raft model for indentation with adhesion. Nature 320, 342–344.

Ghasri-Khouzani, M., McDermid, J.R., 2015. Effect of carbon content on the mechanical properties and microstructural evolution of Fe–22Mn–C steels. Mater. Sci. Eng.: A 621, 118–127.

Gludovatz, B., Hohenwarter, A., Catoor, D., Chang, E.H., George, E.P., Ritchie, R.O., 2014. A fracture-resistant high-entropy alloy for cryogenic applications. Science 345, 1153–1158.

Gouldstone, A., Van Vliet, K.J., Suresh, S., 2001. Nanoindentation: simulation of defect nucleation in a crystal. Nature 411, (656–656).

Gutierrez-Urrutia, I., Raabe, D., 2012. Grain size effect on strain hardening in twinning-induced plasticity steels. Scr. Mater. 66, 992–996.

Gutierrez-Urrutia, I., Zaefferer, S., Raabe, D., 2010. The effect of grain size and grain orientation on deformation twinning in a Fe-22 wt% Mn-0.6 wt% C TWIP steel. Mater. Sci. Eng. A 527, 3552–3560.

Hartley, C.S., Blachon, D.L.A., 1978. Reactions of slip dislocations at coherent twin boundaries in face-centered-cubic metals. J. Appl. Phys. 49, 4788–4796.

Hirsch, P.B., 1962. Extended jogs in dislocations in face-centred cubic metals. Philos. Mag. 7, 67–93.

Hirth, J.P., Hoagland, R.G., 1998. Extrinsically dissociated dislocations in simulated aluminium. Philos. Mag. A 78, 529–532.

J.P. Hirth, J.L., 1982. Theory of Dislocations. Wiley, New York.

Jacobsen, K.W., Schiotz, J., 2002. Computational materials science: nanoscale plasticity. Nat. Mater. 1, 15–16.

Johnson, R.A., 1989. Alloy models with the embedded-atom method. Phys. Rev. B 39, 12554–12559.

Kibey, S., Liu, J.B., Johnson, D.D., Sehitoglu, H., 2006. Generalized planar fault energies and twinning in Cu-Al alloys. Appl. Phys. Lett. 89, 191911–191911-191913.

Kibey, S., Liu, J.B., Johnson, D.D., Sehitoglu, H., 2007. Predicting twinning stress in fcc metals: linking twin-energy pathways to twin nucleation. Acta Mater. 55, 6843–6851.

Kim, S.M., Buyers, W.J.L., 1978. Vacancy formation energy in iron by positron annihilation. J. Phys. F 8, L103.

Li, X., Wei, Y., Yang, W., Gao, H., 2009. Competing grain-boundary- and dislocation-mediated mechanisms in plastic strain recovery in nanocrystalline aluminum. Proc. Natl. Acad. Sci. USA 106, 16108–16113.

Li, X., Wei, Y., Lu, L., Lu, K., Gao, H., 2010. Dislocation nucleation governed softening and maximum strength in nano-twinned metals. Nature 464, 877–880.

Liu, X.Y., Liu, C.L., Borucki, L.J., 1999. A new investigation of copper's role in enhancing Al–Cu interconnect electromigration resistance from an atomistic view. Acta Mater. 47, 3227–3231.

Mahajan, S., Chin, G.Y., 1973. Formation of deformation twins in f.c.c. crystals. Acta Metall. 21, 1353–1363.

Medvedeva, N.I., Park, M.S., Van Aken, D.C., Medvedeva, J.E., 2014. First-principles study of Mn, Al and C distribution and their effect on stacking fault energies in fcc Fe. J. Alloy. Compd. 582, 475–482.

Mendelev, M.I., Srolovitz, D.J., 2002. Determination of alloy interatomic potentials from liquid-state diffraction data. Phys. Rev. B 66, 014205.

Mendelev, M.I., Kramer, M.J., Becker, C.A., Asta, M., 2008. Analysis of semi-empirical interatomic potentials appropriate for simulation of crystalline and liquid Al and Cu. Philos. Mag. 88, 1723–1750.

Mendelev, M.I., Han, S., Srolovitz, D.J., Ackland, G.J., Sun, D.Y., Asta, M., 2003. Development of new interatomic potentials appropriate for crystalline and liquid iron. Philos. Mag. 83, 3977–3994.

Milstein, F., Fang, H.E., Marschall, J., 1994. Mechanics and energetics of the Bain transformation. Philos. Mag. A 70, 621–639.

Mishin, Y., Farkas, D., Mehl, M.J., Papaconstantopoulos, D.A., 1999. Interatomic potentials for monoatomic metals from experimental data and *ab initio* calculations. Phys. Rev. B 59, 3393–3407.

Pierce, D.T., 2012. The Influence of Manganese Content and Temperature on the Relative FCC/HCP Phase Stability and Strain-Hardening Behavior of High-Manganese TRIP/TWIP Steels (Thesis).

Pierce, D.T., Jiménez, J.A., Bentley, J., Raabe, D., Oskay, C., Wittig, J.E., 2014. The influence of manganese content on the stacking fault and austenite/ε-martensite interfacial energies in Fe–Mn–(Al–Si) steels investigated by experiment and theory. Acta Mater. 68, 238–253.

Plimpton, S., 1995. Fast Parallel Algorithms for Short-Range Molecular Dynamics. J. Comput. Phys. 117, 1–19.

Rohatgi, A., Vecchio, K.S., Gray, I.G.T., 2001. A metallographic and quantitative analysis of the influence of stacking fault energy on shock-hardening in Cu and Cu–Al alloys. Acta Mater. 49, 427–438.

Rose, J.H., Smith, J.R., Guinea, F., Ferrante, J., 1984. Universal features of the equation of state of metals. Phys. Rev. B 29, 2963–2969.

Shen, Y.F., Jia, N., Wang, Y.D., Sun, X., Zuo, L., Raabe, D., 2015. Suppression of twinning and phase transformation in an ultrafine grained 2 GPa strong metastable austenitic steel: experiment and simulation. Acta Mater. 97, 305–315.

Steinmetz, D.R., Jäpel, T., Wietbrock, B., Eisenlohr, P., Gutierrez-Urrutia, I., Saeed–Akbari, A., Hickel, T., Roters, F., Raabe, D., 2013. Revealing the strain-hardening behavior of twinning-induced plasticity steels: theory, simulations, experiments. Acta Mater. 61, 494–510.

Van Swygenhoven, H., 2002. Grain boundaries and dislocations. Science 296, 66–67.

Van Swygenhoven, H., Weertman, J.R., 2006. Deformation in nanocrystalline metals. Mater. Today 9, 24–31.

Van Swygenhoven, H., Derlet, P.M., Froseth, A.G., 2004a. Stacking fault energies and slip in nanocrystalline metals. Nat. Mater. 3, 399–403.

Van Swygenhoven, H., Derlet, P.M., Froseth, A.G., 2004b. Stacking fault energies and slip in nanocrystalline metals. Nat. Mater. 3, 399–403.

Van Swygenhoven, H., Spaczer, M., Caro, A., Farkas, D., 1999. Competing plastic deformation mechanisms in nanophase metals. Phys. Rev. B 60, 22–25.

Vegge, T., Leffers, T., Pedersen, O.B., Jacobsen, K.W., 2001. Atomistic simulations of jog migration on extended screw dislocations. Mater. Sci. Eng. A 319–321, 119–123.

Weixue, L., Tzuchiang, W., 1998. Ab initio investigation of the elasticity and stability of aluminium. J. Phys.: Condens. Matter 10, 9889.

Yamakov, V., Wolf, D., Phillpot, S.R., Mukherjee, A.K., Gleiter, H., 2002. Dislocation processes in the deformation of nanocrystalline aluminium by molecular-dynamics simulation. Nat. Mater. 1, 45–49.

Yamakov, V., Wolf, D., Phillpot, S.R., Mukherjee, A.K., Gleiter, H., 2004. Deformation-mechanism map for nanocrystalline metals by molecular-dynamics simulation. Nat. Mater. 3, 43–47.

Yan, X., Sharma, P., 2016. Time-Scaling in Atomistics and the Rate-Dependent Mechanical Behavior of Nanostructures. Nano Lett. 16, 3487–3492.

Yan, X., Gouissem, A., Sharma, P., 2015. Atomistic insights into Li-ion diffusion in amorphous silicon. Mech. Mater. 91, Part 2, 306–312.

Yip, S., 2004. Nanocrystalline metals: mapping plasticity. Nat. Mater. 3, 11–12.

Zhang, Y., Tao, N.R., Lu, K., 2009. Effect of stacking-fault energy on deformation twin thickness in Cu–Al alloys. Scr. Mater. 60, 211–213.

Zhang, Y., Zuo, T.T., Tang, Z., Gao, M.C., Dahmen, K.A., Liaw, P.K., Lu, Z.P., 2014. Microstructures and properties of high-entropy alloys. Prog. Mater. Sci. 61, 1–93.

Zhou, S.J., Preston, D.L., Louchet, F., 1999. Investigation of vacancy formation by a jogged dissociated dislocation with large-scale molecular dynamics and dislocation energetics. Acta Mater. 47, 2695–2703.

Zhou, S.J., Preston, D.L., Lomdahl, P.S., Beazley, D.M., 1998. Large-scale molecular dynamics simulations of dislocation intersection in copper. Science 279, 1525–1527.

Zhu, Y.T., Liao, X.Z., Wu, X.L., 2012. Deformation twinning in nanocrystalline materials. Prog. Mater. Sci. 57, 1–62.

Zhu, Y.T., Narayan, J., Hirth, J.P., Mahajan, S., Wu, X.L., Liao, X.Z., 2009. Formation of single and multiple deformation twins in nanocrystalline fcc metals. Acta Mater. 57, 3763–3770.

Zhu, Y.T., Wu, X.L., Liao, X.Z., Narayan, J., Kecskés, L.J., Mathaudhu, S.N., 2011. Dislocation–twin interactions in nanocrystalline fcc metals. Acta Mater. 59, 812–821.